THE LOCALIZATION OF PARTICLE ACCELERATION SITES IN SOLAR FLARES AND CMES

MARKUS J. ASCHWANDEN
Solar and Astrophysics Lab., Lockheed Martin ATC, 3251 Hanover St., Palo Alto, CA 94304, USA
(E-mail: aschwanden@lmsal.com)

(Received 21 July 2005; Accepted in final form 7 September 2005)

Abstract. We review the particular aspect of determining particle acceleration sites in solar flares and coronal mass ejections (CMEs). Depending on the magnetic field configuration at the particle acceleration site, distinctly different radiation signatures are produced: (1) If charged particles are accelerated along compact closed magnetic field lines, they precipitate to the solar chromosphere and produce hard X-rays, gamma rays, soft X-rays, and EUV emission; (2) if they are injected into large-scale closed magnetic field structures, they remain temporarily confined (or trapped) and produce gyrosynchrotron emission in radio and bremsstrahlung in soft X-rays; (3) if they are accelerated along open field lines they produce beam-driven plasma emission with a metric starting frequency; and (4) if they are accelerated in a propagating CME shock, they can escape into interplanetary space and produce beam-driven plasma emission with a decametric starting frequency. The latter two groups of accelerated particles can be geo-effective if suitably connected to the solar west side. Particle acceleration sites can often be localized by modeling the magnetic topology from images in different wavelengths and by measuring the particle velocity dispersion from time-of-flight delays.

Keywords: solar flares, coronal mass ejections, particle acceleration

1. Introduction

The knowledge of the location of particle accelerators in the solar corona is important in many respects: (1) to probe the electromagnetic fields and physical conditions in the acceleration region; (2) to predict the (adiabatic) trajectories of accelerated particles; (3) to predict the targets and energy losses of the accelerated particles; (4) to model and diagnose their radiation signatures in many wavelengths; and (5) to understand their origin and chemical composition when detected *in-situ*. In the context of solar flares and coronal mass ejections (CMEs), multi-wavelength images may constrain the magnetic topology at the acceleration site and along the particle trajectories. A powerful tool to constrain the location of particle acceleration sites in solar flares and CMEs is the method of time-of-flight measurements, which can be applied to solar hard X-rays as well as to *in-situ* detections of high-energy particles near 1 AU. We organize this review by considering various magnetic field configurations in the particle acceleration sites, which also can be used as diagnostic for localizing the acceleration sites and particle propagation paths.

Space Science Reviews (2006) 124: 361–372
DOI: 10.1007/s11214-006-9095-9

2. Particle Acceleration in Primary Flare Loops

It is generally believed that solar flares and CMEs are triggered by a magnetic instability in the lower corona, which is often accompanied with the eruption of an unstable filament and involves a magnetic reconnection process (for a summary see, e.g., Aschwanden, 2004, Sections 10–12). The various magnetic topologies can be classified into 2D and 3D configurations, of which the most common ones are the bipolar, tripolar, and quadrupolar geometry (Figure 1). These configurations involve a magnetic topology change between open and closed magnetic field lines, which in all three cases produce a compact post-reconnection field line, which we call the *"primary flare loop"*. Let us consider first the fate of accelerated particles in those primary flare loops, which consist of compact closed magnetic field lines.

The geometric reconstruction of the pre-reconnection field lines can be accomplished for each (new) post-reconnection field line (marked with double linestyle in Figure 1) by switching the magnetic polarities to obtain the alternative (old) connectivity (marked with dashed linestyle in Figure 1). This geometric reconstruction implies that each post-reconnection field line relaxes from a cusp-shaped field line (during reconnection) into a circular post-reconnection field line. The shortening from the cusp-shaped to the circular field line yields the free magnetic energy ΔW (per cross-sectionional area dA) that can be dissipated,

$$\frac{\Delta W}{dA} \approx \int_{\text{cusp}} \frac{B^2(s')}{8\pi} ds' - \int_{\text{relaxed}} \frac{B^2(s)}{8\pi} ds \approx \frac{\langle B \rangle^2}{8\pi}(s' - s) > 0. \tag{1}$$

The cusp area that is outlined during the shrinkage of the field line demarcates the primary acceleration site (marked with a hatched area in the third row in Figure 1). The altitude h_{acc} of the acceleration site in the cusp region has also been confirmed from electron time-of-flight (TOF) measurements between the coronal cusp and chromospheric footpoints, which was found to scale with the loop height $h_{\text{loop}} = L_{\text{halfloop}} \times (2/\pi)$ by

$$\frac{h_{\text{acc}}}{h_{\text{loop}}} \approx \frac{L_{\text{TOF}}}{L_{\text{halfloop}}} = 1.43 \pm 0.30, \tag{2}$$

based on energy-dependent hard X-ray time delays (Aschwanden *et al.*, 1996). The relaxation process implies that the accelerated particles are confined to the relaxing compact (primary) field line and have no escape possibility. Therefore, the accelerated particles have no other choice than to precipitate to the two footpoints of the primary postflare loop, either directly (within a half loop transit time) or after several mirror reflections as a consequence of wave-induced or collision-induced pitch angle scattering. The precipitating electrons are then stopped in the chromosphere and produce collisional bremsstrahlung in hard X-rays. The accelerated

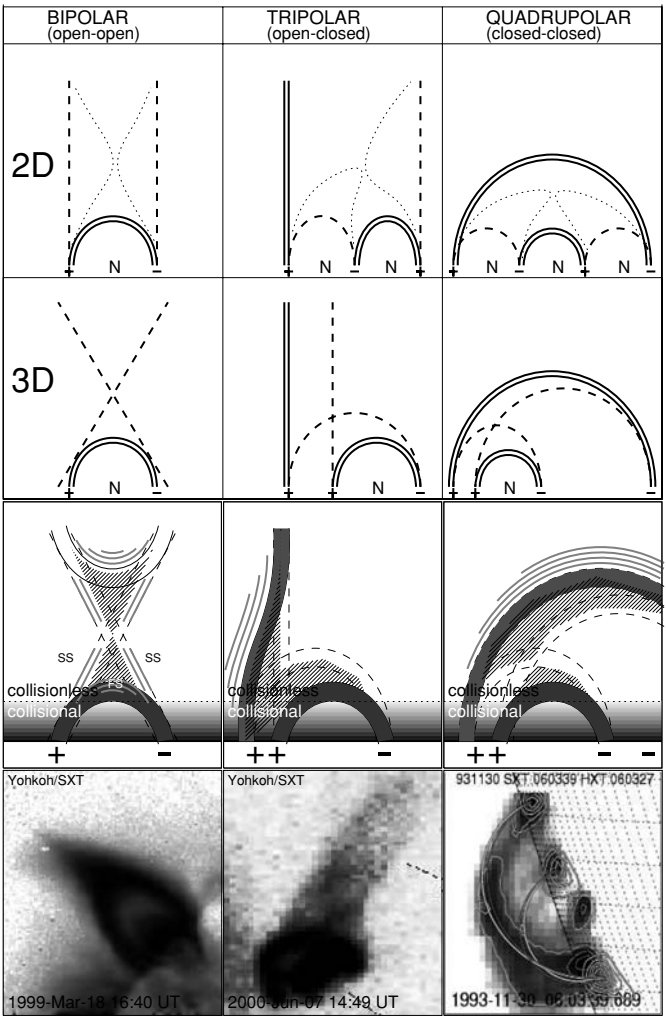

Figure 1. The topology of magnetic reconnection regions is classified into three combinations: bipolar or open-open (left column), tripolar or open-closed (middle column), and quadrupolar or closed-closed field line reconnection (right column). The 2D versions are shown in the top row, with the pre-reconnection field lines marked with dashed lines, during reconnection with dotted lines, and post-reconnection field lines with double solid linestyle. The 3D versions are indicated in the second row, where the pre-reconnection field lines are not coplanar, but located behind each other. The third row indicates the acceleration regions (hatched), the relative densities (greyscale), and upward/sideward directed shocks (grey lines). The bottom row shows flare observations from Yohkoh/SXT that correspond to the three different reconnection topologies (adapted from Aschwanden, 2004).

ions precipitate also but produce nuclear de-excitation lines in gamma-rays in the chromosphere. The relativistic electrons produce also gyrosynchrotron emission in radio wavelengths, which is generally delayed by seconds to minutes depending on the trapping time, which increases with (relativistic) energy.

None of these energized particles accelerated in the relaxing primary flare loop can escape into the upper corona and interplanetary space, but their sharply defined timing can often be used to determine the time at which energized particles are injected into secondary magnetic field lines, concomitantly accelerated in the same reconnection process, possibly injected onto an escape route into interplanetary space. The particles accelerated in the primary flare loop are therefore an independent population and magnetically decoupled from *solar energetic particles (SEPs)* that are detected in the heliosphere or near Earth. So, the two populations of high-energy particles have a different origin and are not expected to have the same energy or spectra.

3. Particle Acceleration in Secondary Flare Loops

The quadrupolar configuration (Figure 1, right-hand side) involves magnetic reconnection between two closed magnetic field lines, which relaxes into an alternative quadrupolar connection with switched polarities. This basic (3D) quadrupolar reconnection process has also been dubbed as a flaring process between *"two interacting loops"* and was physically interpreted as a magnetic flux transfer between two current-carrying loops (Melrose, 1997). Observational evidence for this type of reconnection was obtained from the detailed analysis of magnetic polarities at the flare loop footpoints (Hanaoka, 1996, 1997; Nishio *et al*., 1997) and the 3D reconstruction of the magnetic field topology (Aschwanden *et al*., 1999). In most of the cases observed by Hanaoka (1996, 1997) and Nishio *et al*. (1997), the secondary large-scale flare loop showed a brightening in soft X-rays and microwaves (see the four cases in Figure 2), simultaneously with the bright hard X-ray and soft X-ray emission in the primary (compact) flare loop, which strongly suggests a simultaneous injection of accelerated particles into the secondary (large-scale) loop. The injection of energized particles is likely to be accomplished from the common reconnection X-point, where acceleration is likely to occur in the upward-located cusp that is outlined by the relaxation of the secondary flare loop. The secondary flare loop generally is substantially bigger and thus the injected heated plasma and the number of accelerated particles is spread over a larger volume, causing fainter bremsstrahlung emission in soft X-rays and gyrosynchrotron emission in microwaves than from the (compact) primary flare loop. Also, hard X-ray emission has not been detected (or only at a very weak level) at the remote footpoint of the secondary flare loop, probably because the propagating electrons become mirrored or lose gradually their energy on the way to the remote footpoint. However, the relativistic speed of accelerated electrons in these secondary flare loops has been measured from time-of-flight measurements between the injection point and the remote footpoint (e.g., Hanaoka, 1999; Lang and Willson, 1989).

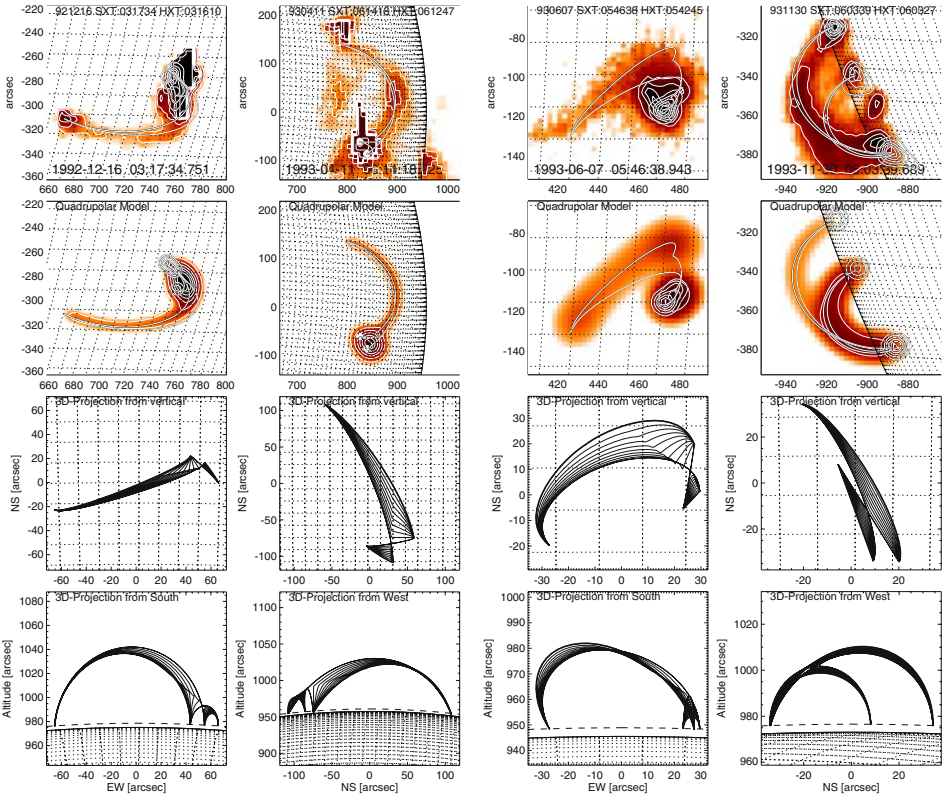

Figure 2. Reconstruction of reconnection geometry with a 3D quadrupolar model: *Top row:* soft X-ray image (logarithmic greyscale and thin contours) from Yohkoh/SXT and hard X-ray image (thick contours) from Yohkoh/HXT. The thin circular segments represent the pre-reconnection field lines, and the thick circular segments show the corresponding post-reconnection field lines, which coincide with the flare loops. *Second row:* simulated SXR and HXR maps constrained by the 3D quadrupolar model (shown in Figure 1), represented by identical greyscales and contour levels just like the original data (in the top row). *Third row:* the geometric solution of the 3D quadrupolar model is rotated so that the vertical z-axis coincides with the line-of-sight. Ten field lines are interpolated between the pre-reconnection and post-reconnection state, visualizing the relaxation process of field lines after reconnection. *Bottom row:* the same 3D model is rotated so that either the x-axis (view from west) or the y-axis (view from south) coincides with the line-of-sight. The spacing of the heliographic grid is 1° in all frames, corresponding to 12,150 km (Aschwanden *et al.*, 1999).

Other examples of particle acceleration in large-scale, closed magnetic field geometries comes from radio type-U bursts, which are likely to represent secondary flare loops as described above. The U-type morphology indicates the propagation of electron beams along closed magnetic field lines. A case of a U-burst that has also been simultaneously imaged with the *Very Large Array (VLA)* is shown in Figure 3. The turnover frequency of the type U-burst in the dynamic spectra corresponds to

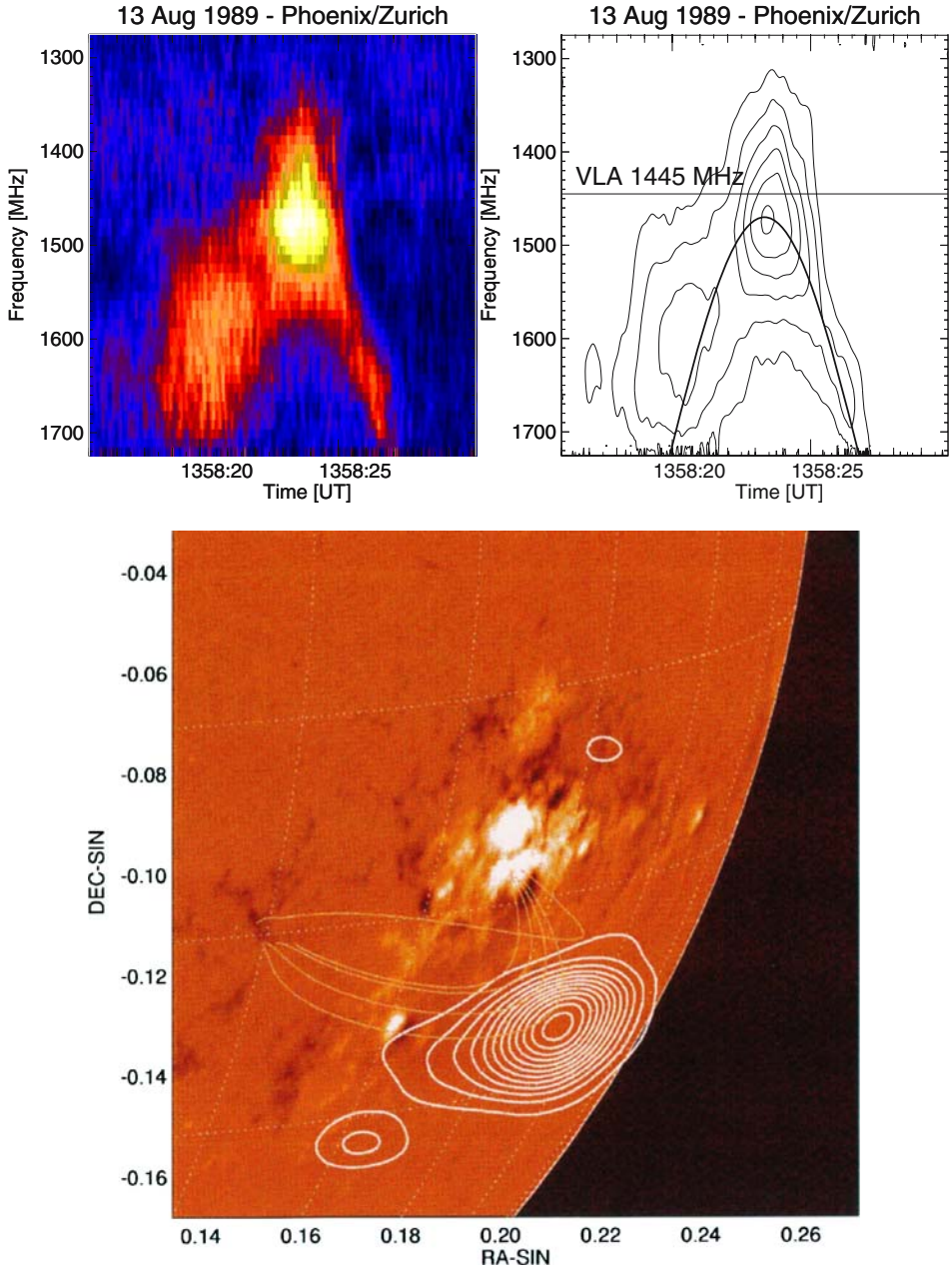

Figure 3. Top: Radio observations of a type U-burst on 1989-Aug-13 with the ETH Zurich spectrometer. The dynamic spectrum (frequency versus time) shows a duration of ≈7 s and a turnover frequency of $\nu \approx 1.5$ GHz for the U-burst. *Bottom:* The turnover of the U-burst was simultaneously imaged with the VLA at a frequency of $\nu = 1.445$ GHz. A potential magnetic field extrapolation at the same location based on a KPNO/NSO magnetogram confirms the presence of closed magnetic field lines (thin curves) at the location of the U-burst (Aschwanden *et al.*, 1992).

$\nu \approx 1.5$ GHz, which accidentally was also close to the imaging frequency of the VLA. A magnetic field extrapolation at the location of the U-burst turnover location confirmed that the radio source was confined at the top of closed magnetic field lines (Aschwanden *et al*., 1992). The U-burst might well be part of a quadrupolar configuration, with the compact primary loop located near the footpoint of the (western) leading sunspot.

Since the secondary loop in a quadrupolar configuration represents a closed magnetic field line, no accelerated particle can escape into the upper corona or into interplanetary space, and thus they are magnetically decoupled from SEP particles detected in the heliosphere or near Earth. Actually, since both the primary and secondary flare loops are closed in quadrupolar configurations, we do not expect any common acceleration site for solar flare particles and SEPs in such quadrupolar events. This might also explain why a number of large flares seem to have fully confined magnetic topologies, which produce strong gamma-rays but completely lack radio emission (e.g., Simnett and Benz, 1986; Rieger *et al*., 1999).

4. Particle Acceleration in Open Magnetic Fields

Energetic particles accelerated in solar flares can only escape into interplanetary space if some open magnetic fields are involved in the magnetic reconnection process. Both the bipolar and tripolar case (Figure 1, left and middle column) involve open pre-reconnection field lines. In addition, the tripolar case (Figure 1, middle column) transforms again to an open post-reconnection field line. While the three reconnection topologies shown in Figure 1 encompass only basic components between two reconnecting field lines, a real flare may be considered as a temporal sequence of many such basic reconnection processes, which can occur in arbitrary sequences, and thus most flares may involve a time phase where open field lines are involved. For instance, a flare may start with reconnection of highly-sheared low-lying field lines above the neutral line that are all closed (i.e., quadrupolar) initially, while it may later evolve into reconnection of less-sheared high-lying field lines that could involve open field lines at some particular locations (i.e., tripolar). Such a flare would initially confine the accelerated particles, but inject them into interplanetary space in a later phase. A temporary opening of the magnetic field configuration is, for instance, envisioned in the so-called *"magnetic break-out"* flare model (Antiochos *et al*., 1999).

On the other hand, open field regions that connect directly to the interplanetary space exist not only in coronal holes, but also to a substantial fraction in active regions (Figure 4). Schrijver and DeRosa (2003) found from potential-field extrapolations of the global magnetic field over the entire solar surface that the *interplanetary magnetic field (IMF)* originates typically in a dozen disjoint regions, around the solar cycle maximum. While active regions are often ignored as a source for the interplanetary magnetic field, Schrijver and DeRosa (2003) found that the fraction of the IMF that connects directly to magnetic plages of active regions in-

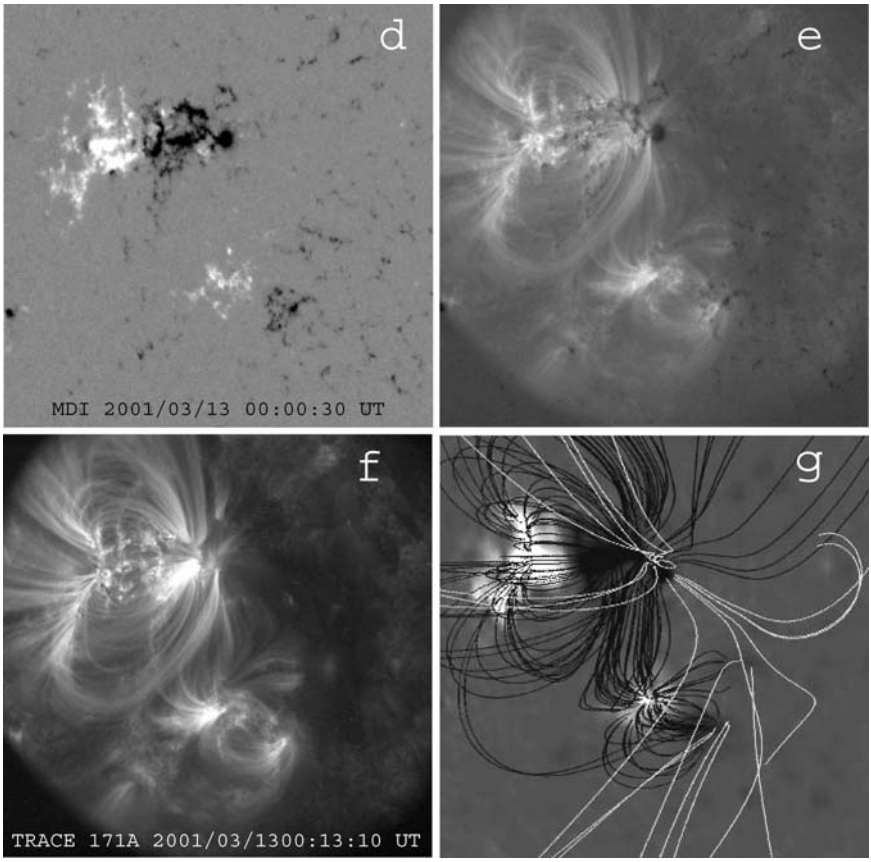

Figure 4. Top left: Magnetogram recorded with the *Michelson Doppler Imager (MDI)* onboard the *Solar and Heliospheric Observatory (SoHO)*; *Top right: MDI* magnetogram overlayed on an EUV 171 Å image from the *Transition Region and Coronal Explorer (TRACE)*; *Bottom left:* TRACE 171 Å image of 2001-Mar-13, 00:13 UT; *Bottom right:* Potential field extrapolation using a source-surface model. Closed field lines of active regions are indicated with black color, the open field lines that connect to interplanetary space with white. The spatial scale of a panel is a half solar radius (350,000 km), (courtesy of Schrijver and DeRosa, 2003).

creases from $\lesssim$10% at cycle minimum up to 30–50% at cycle maximum, with even direct connections between sunspots and the heliosphere (Figure 4). Additional support for the magnetic connectivity comes also also from the establishment of a connection between the interplanetary field and active region fields (Neugebauer *et al.*, 2002; Liewer *et al.*, 2004).

The most common diagnostic of particle acceleration along open magnetic field lines are radio type III bursts, which are detected in the majority of flares. For flare-associated acceleration at coronal heights we expect decimetric starting frequencies (corresponding to electron densities of $n_e \gtrsim 10^9$ cm^{-3}) or metric starting frequencies ($n_e \gtrsim 10^8$ cm^{-3}), which both may have extensions to interplanetary type III

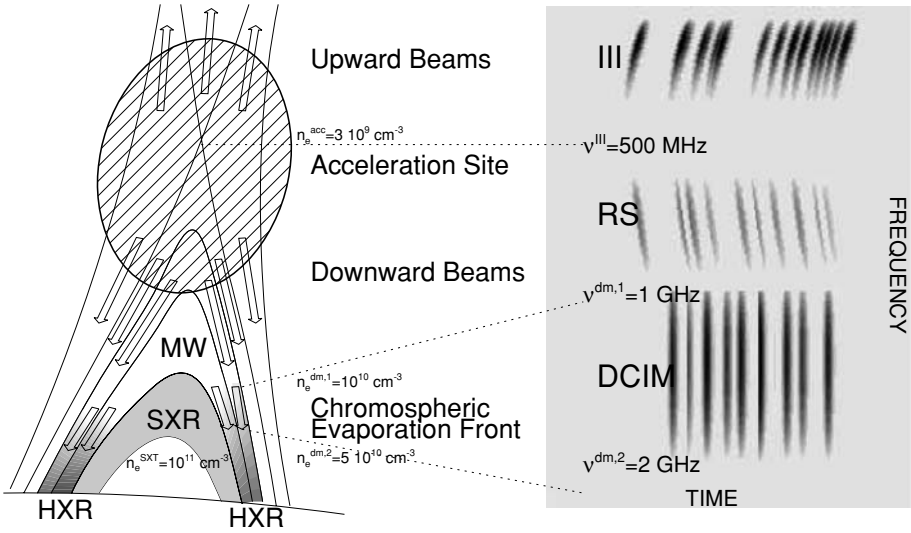

Figure 5. A diagram of a flare model is shown, inferred from the magnetic topology constraint of simultaneously detected upward and downward electron beams, in radio and hard X-rays. The diagram on the right illustrates a dynamic radio spectrum with radio bursts indicated in the frequency-time plane. The acceleration site is located in a low-density region (in the cusp) with a density of $n_e^{\rm acc} \approx 10^9$ cm^{-3} from where electron beams are accelerated in upward (type III) and downward (RS bursts) directions. Downward-precipitating electron beams produce pulses of chromospheric thick-target bremsstrahlung emission, possibly intercepting chromospheric upflows. Those loops that have already been filled with heated chromospheric plasma brighten up in soft X-rays and have higher densities of $n_e^{\rm SXR} \approx 10^{11}$ cm^{-3} than the acceleration region. There is a filling delay of soft X-ray loops, during which the magnetic reconnection point rises higher, widening the hard X-ray emitting footpoints (Aschwanden and Benz, 1997).

bursts (but not always). Inversely, however, almost all interplanetary type III bursts are found to be rooted in coronal type III bursts (e.g., Poquérusse *et al.*, 1996). So, the localization of acceleration regions along open magnetic field lines can be constrained from the electron density that corresponds to the (fundamental) plasma frequency of the starting frequency of type III bursts, which is often found around $n_e \approx 10^9$ cm^{-3} (Aschwanden and Benz, 1997), and thus most likely corresponds to the upward-directed cusp of reconnection X-points in coronal flare sites (Figure 5).

5. Particle Acceleration in CMEs

Besides the flare-associated acceleration sites described above, there are also CME-associated acceleration sites, produced in the shocks associated with super-Alfvénic CME fronts that propagate through interplanetary space. CMEs have speeds from

20 to 2500 km s^{-1}. The fast CMEs with speeds in excess of the ambient solar wind ($\gtrsim$800 km s^{-1}) drive shocks ahead and are capable of accelerating particles. Recent numerical simulations of realistic CME shocks show that the diffusive shock acceleration process can accelerate solar energetic protons up to energies of 10 GeV (Roussev *et al.*, 2004; Manchester *et al.*, 2005; Kocharov *et al.*, 2005; Tsurutani *et al.*, 2003). The acceleration efficiency, however, varies considerably along a circular CME shock wave, depending on the angle between the shock normal and the incident magnetic field. Quasi-perpendicular shocks, which are found at the outer flanks of CMEs, accelerate particles at a higher rate than quasi-parallel shocks, supposedly occurring near the CME front (Giacalone, 2005a, b).

Solar energetic particle (SEP) events detected at Earth are subdivided into *impulsive* and *gradual events*, of which the latter type clearly originates from CME-driven shocks during propagation from the corona through the heliosphere (Reames, 1999; Kahler, 2001). SEP events detected near Earth indicate magnetic connectivity between the CME site and the Earth, a necessary condition for *geo-effective events*. CME shocks accelerate at least two different seed populations, flare suprathermals as well as solar-wind particles. Distinctive differences in the elemental composition suggest that quasi-parallel shocks (in the CME front) generally draw their seeds from solar-wind suprathermals, while quasi-perpendicular shocks (in the CME flanks) preferentially accelerate flare supra-thermals, because they require a higher initial speed for effective injection (Tylka *et al.*, 2005).

The acceleration site of CME-accelerated particles can also be determined with time-of-flight measurements of their velocity dispersion. Recent measurements with the *Wind* spacecraft have shown two classes of accelerated protons: one class that traveled essentially scatter-free over a path length of $\approx$1.1–1.3 AU, while the other shows a path length of $\approx$2.0 AU. The first class seems to be accelerated in the range of $\approx 1-10\ R_{\odot}$, while the second class seems to be accelerated successively later (Krucker *et al.*, 1999; Krucker and Lin, 2000).

Since the plasma in interplanetary space is collisionless, superthermal and high-energy particles can propagate through interplanetary space and form particle beams that are responsible for *interplanetary radio type III bursts*. There is also a particular type of interplanetary type III-like bursts, called *"shock-associated (SA) events"*, believed to be electron beams that are produced by collisionless shocks associated with passing CMEs and propagate in the antisunward direction from the (type II-emitting) shock (Cane *et al.*, 1981). Radio type II emission is the most common signature of shocks propagating in the corona and interplanetary space, and thus is used as a robust diagnostic of propagating CMEs. Enhanced radio emission and SEP production is observed when a fast CME passes a slow CME, which is interpreted as a consequence of shock strengthening (Gopalswamy *et al.*, 2001, 2002). Occasionally, there occur also interplanetary radio type IV-like bursts, i.e., synchrotron emission caused by energetic electrons confined in a magnetic trap

created behind an interplanetary shock wave (Bastian *et al.*, 2001). The spatial size of interplanetary radio bursts can be very large, since the extent of the radio source grows with distance from the Sun. Nevertheless, radio imaging at multiple frequencies aids to reconstruct the CME-associated acceleration sites and particle kinematics.

6. Final Remarks

The acceleration sites of electrons in flares have been identified in the immediat neighborhood of magnetic reconnection sites, based on electron time-of-flight measurements and coronal hard X-ray emission, but we have much less diagnostics on the acceleration sites of ions. The acceleration sites of energetic particles in CMEs are less known for several reasons: (1) we are lacking accurate magnetic field models in CME environments, (2) the method of velocity dispersion applied to distances of 1 AU has uncertainties in the order of solar radii, and (3) *in-situ* detection of particles is mostly carried out at distances of 1 AU. The STEREO mission will constrain particle acceleration sites in CMEs significantly better.

Acknowledgements

Part of the work was supported by NASA contract NAS5-98033 (RHESSI mission) through University of California, Berkeley (subcontract SA2241-26308PG) and the NASA contract NAS5-38099 (TRACE mission). Workshop participation was supported by the *International Space Science Institute (ISSI)*, Bern, Switzerland.

References

Antiochos, S. K., DeVore, C. R., and Klimchuk, J. A.: 1999, *ApJ* **510**, 485.

Aschwanden, M. J., Bastian, T. S., Benz, A. O., and Brosius, J. W.: 1992, *ApJ* **391**, 380.

Aschwanden, M. J., Wills, M. J., Hudson, H. S., Kosugi, T., and Schwartz, R. A.: 1996, *ApJ* **468**, 398.

Aschwanden, M. J., and Benz, A. O.: 1997, *ApJ* **480**, 825.

Aschwanden, M. J., Kosugi, T., Hanaoka, Y., Nishio, M., and Melrose, D. B.: 1999, *ApJ* **526**, 1026.

Aschwanden, M. J.: 2002, *Space Sci. Rev.* **101**(1–2), 1.

Aschwanden, M. J.: 2004, *Physics of the Solar Corona – An Introduction*, Praxis Publishing Ltd., Chichester UK, and Springer, New York, ISBN 3-540-22321-5, 842 p.

Aschwanden, M. J.: 2005, in Gopalswamy, N., Mewaldt, R., and Torsti, J. (eds.), AGU Monograph "Solar Eruptions and Energetic Particles", Vol. 165, p. 189.

Bastian, T. S., Pick, M., Kerdraon, A., Maia, D., and Vourlidas, A.: 2001, *ApJ* **558**, L65.

Cane, H. V., Stone, R. G., Fainberg, J., Stewart, R. T., Steinberg, J. L., and Hoang, S.: 1981, *JGR* **8/12**, 1285.

Giacalone, J.: 2005a, *ApJ* **624**, 765.

Giacalone, J.: 2005b, *ApJ* **628**, L73.
Gopalswamy, N., Yashiro, S., Kaiser, M. L., Howard, R. A., and Bougeret, J.: 2001, *ApJ* **548**, L91.
Gopalswamy, N., Yashiro, S., Michalek, G., Kaiser, M. L., Howard, R. A., Reames, D. V., *et al.*: 2002, *ApJ* **572**, L103.
Hanaoka, Y.: 1996, *Solar Phys.* **165**, 275.
Hanaoka, Y.: 1997, *Solar Phys.* **173**, 319.
Hanaoka, Y.: 1999, *Publ. Astron. Soc. Japan* **51**, 483.
Kahler, S. W.: 2001, *JGR* **106/A10**, 20947.
Kocharov, L., Lytova, M., Vainio, R., Laitinen, T., and Torsti, J.: 2005, *ApJ* **620**, 1052.
Krucker, S., Larson, D. E., Lin, R. P., and Thompson, B. J.: 1999, *ApJ* **519**, 864.
Krucker, S., and Lin, R. P.: 2000, *ApJ* **542**, L61.
Lang, K. R., and Willson, R. F.: 1989, *ApJ* **344**, L77.
Liewer, P. C., Neugebauer, M., and Zurbuchen, T.: 2004, *Solar Phys.* **223**, 209.
Manchester, W. B., Gombosi, T. I., De Zeeuw, D. L., Sokolov, I. V., Roussev, I. I., Powell, K. G., *et al.*: 2005, *ApJ* **622**, 1225.
Melrose, D. B.: 1997, *ApJ* **486**, 521.
Neugebauer, M., Liewer, P. C., Smith, E. J., Skoug, R. M., and Zurbuchen, T. H.: 2002, *JGR* (Space Physics) **107**, Issue A12, pp. SSH 13-1, CiteID 1488, DOI 10.1029/2001JA000306.
Nishio, M., Yaji, K., Kosugi, T., Nakajima, H., and Sakurai, T.: 1997, *ApJ* **489**, 976.
Poquérusse, M., Hoang, S., Bougeret, J. L., and Moncuquet, M.: 1996, in Winterhalter, D., Gosling, J. T., Habbal, S. R., Kurth, W. S., and Neugebauer, M. (eds.), *Solar Wind Eight*, Internat. Solar Wind Conference, held in Dana Point, California, June 1995, AIP Press, New York, American Institute of Physics Conference Proceedings AIP CP-382, pp. 62–65.
Reames, D. V.: 1999, *Space Sci. Rev.* **90**, 413.
Rieger, E., Treumann, R. A., and Karlicky, M.: 1999, *Solar Phys.* **187**, 59.
Roussev, I. I., Sokolov, I. V., Forbes, T. G., Gombosi, T. I., Lee, M. A., and Sakai, J. I.: 2004, *ApJ* **605**, L73.
Schrijver, C. J., and DeRosa, M. L.: 2003, *Solar Phys.* **212**, 165.
Simnett, G. M., and Benz, A. O.: 1986, *Astron. Astrophys.* **165**, 227.
Tsurutani, B. T., Wu, S. T., Zhang, T. X., and Dryer, M.: 2003, *Astron. Astrophys.* **412**, 293.
Tylka, A. J., Cohen, C. M. S., Dietrich, W. F., Lee, M. A., Maclennan, C. G., Mewaldt, R. A., *et al.*: 2005, *ApJ* **625**, 474.